Since January 2020 Elsevier has created a COVID-19 resource centre with free information in English and Mandarin on the novel coronavirus COVID-19. The COVID-19 resource centre is hosted on Elsevier Connect, the company's public news and information website.

Elsevier hereby grants permission to make all its COVID-19-related research that is available on the COVID-19 resource centre - including this research content - immediately available in PubMed Central and other publicly funded repositories, such as the WHO COVID database with rights for unrestricted research re-use and analyses in any form or by any means with acknowledgement of the original source. These permissions are granted for free by Elsevier for as long as the COVID-19 resource centre remains active.

Journal of Hazardous Materials 403 (2021) 123909

Contents lists available at ScienceDirect

Journal of Hazardous Materials

journal homepage: www.elsevier.com/locate/jhazmat

Bioinspired synthesis of fiber-shaped silk fibroin-ferric oxide nanohybrid for superior elimination of antimonite

Pengfei Qi [a,*], Jianqiang Zeng [a], Xiaohua Tong [a], Junjie Shi [b,c], Yan Wang [d], Kunyan Sui [a,*]

[a] State Key Laboratory of Bio-Fiber and Eco-textiles, College of Materials Science and Engineering, Collaborative Innovation Center for Marine Biobased Fibers and Ecological Textiles, Institute of Marine Biobased Materials, Qingdao University, No. 308 Ningxia Road, Qingdao, 266071, China
[b] School of Chemistry & Chemical Engineering, Yantai University, Yantai, 264005, China
[c] Department of Chemical Engineering, University of Florida, Gainesville, Florida, 32611, United States
[d] College of Chemistry and Chemical Engineering, Qingdao University, Qingdao 266071, China

ARTICLE INFO

Editor: G. Lyberatos

Keywords:
Silk nanofibril/ferric oxide nanohybrids
Advanced antimonite capturing
High selectivity

ABSTRACT

Bioinspired fibrous materials have emerged as a unique class of matrix for fabrication of fiber-shaped nanomaterial assemblies. Here, we report a novel functional fiber-shaped nanohybrid for efficient removal of antimonite via in situ synthesis of ferric oxides anchored to silk nanofibril. The silk nanofibril matrix played important roles in the growth of ferric oxides via metal-ligand interactions. The achieved nanocomposites had high surface areas and activity with more functional groups, contributing to superior antimonite elimination. The nanocomposite achieved a maximum removal capacity of 159.9 mg/g toward antimonite. And the common interfering ions of SO_4^{2-}, NO_3-, CO_3^{2-}, PO_4^{3-} and SiO_3^{2-} exhibited negligible influence on antimonite removal. The mechanism study point that two factors are closely involved: surface complexation and hydrogen bonding. Benefiting from the low cost and environmental-friendly nature of silk fibroin as well as excellent removal capacity and high selectivity, it suggests that the nanohybrids might be promising for antimonite extraction from contaminated water.

1. Introduction

Polluted natural environment and ecological imbalance could bring disastrous loss and harsh living conditions, for example, the proliferating Novel Coronavirus around the whole world in 2020. As the source of life, safe and clean drinking water is crucial for human life and health, however, the water quality is deteriorated due to natural processes and anthropological activities. Thus, this is especially urgent to capture the highly toxic heavy metals which are easy to migrate and accumulate in organisms such as antimonite. Antimonite, generally existed as $Sb(OH)_3$, is the most toxic species of antimony. Among the existing removal technologies, adsorption is still one of the most intriguing methods for antimony removal involving strong practicality, simplicity and high efficiency (Zhang et al., 2019a). However, the removal efficiency is still not satisfying. Thus, the development of environmental-friendly and low-cost materials with high antimonite loading capacity are highly desirable.

Recently, various kinds of nano materials have been developed for antimony removal, including metal organic frameworks (Qi et al., 2019; Li et al., 2017; Li et al., 2018), titanate nanotube (Zhao et al., 2019; Liu et al., 2019) and nanosized metal (hydro)oxides such as iron, zirconium and manganese oxides (Zeng et al., 2020; Luo et al., 2017a; Wang et al., 2014). The most representative of nanostructured ferric oxides have attracted significant attention for capturing of antimonite due to the properties of low cost, high abundance, large surface area and high reactivity (Ungureanu et al., 2015). However, the natural nanostructured ferric oxides may instable and transfer to other types of iron oxides with good crystallinity, leading to a lower surface area and lower reactivity. Manipulating the structure and morphology of the ferric oxide using templates could be reasonable to enhance the removal capacity for antimonite. For example, iron oxide was loaded on the biochar fiber to prepare a nanoneedle type of composite with high adsorption capacity for As(V) (Wei et al., 2019). The hydrated ferric oxide nanoparticles encapsulated inside porous matrixes such as resins and granular activated carbon had a stronger binding ability with Cu(II) ions than the pure hydrated ferric oxides (Pan et al., 2018). Among these templates, natural fibers could exhibit special properties due to their large surface areas and high surface-volume ratio. And it could be feasible to

* Corresponding authors.
E-mail addresses: pengfei@uni-bremen.de (P. Qi), sky@qdu.edu.cn (K. Sui).

https://doi.org/10.1016/j.jhazmat.2020.123909
Received 19 July 2020; Received in revised form 7 September 2020; Accepted 8 September 2020
Available online 11 September 2020
0304-3894/© 2020 Elsevier B.V. All rights reserved.

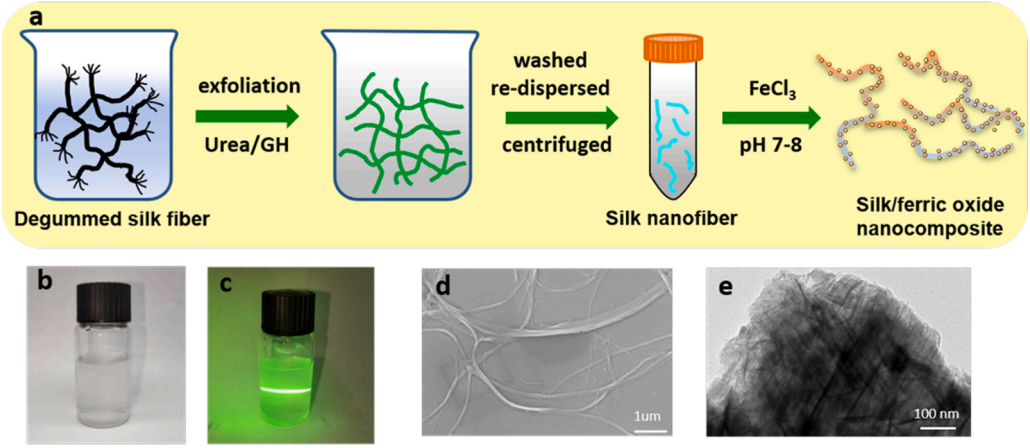

Fig. 1. (a) Schematic illustration of the fabrication of silk fibroin-ferric oxide nanocomposite. (b) Photographs of aqueous suspension of exfoliated SNFs. (c) SEM images of SNF. (d) TEM image of SNF/ferric oxide composite.

enhance the removal capacity of antimonite by the functional nanohybrid combining the properties of natural fibers and ferric oxides.

Silk fibroin (SF) is a natural polymer extracted from *Bombyx mori* silkworm containing abundant amino acid residues and deserving unique hierarchical structures (Rockwood et al., 2011; Wang et al., 2018a). The silk fibroin has unique sequence self-assembly behaviors with abundant hydrophilic moieties such as hydroxyl groups, carboxyl groups, amino groups and acylamino groups, which are prone to assemble with metal ions and small molecular to design novel nanohybrids such as Fe_3O_4/SF nanoparticles (Sheng et al., 2014; Samal et al., 2015), hematite (Fei et al., 2013a), copper oxide (Fei et al., 2013b), hydroxyapatite (Mi et al., 2016), SF/silver nanowire composite (Xue et al., 2019) and Au nanoparticles@SF hybrid materials (Shi et al., 2019). Also, the various amine-based functional groups are beneficial in the removal of heavy metals (Gore et al., 2019). Nowadays, the silk nanofibril was usually obtained by dissolving the silk fibroin in high concentrated salt solution or in a ternary organic/inorganic solvent and then dialyzing it, however, the silk nanofibrils obtained by the strong degradation methods are not easy to control and could generate random coils. More unfortunately, there has been no study reported on the capture of antimonite by the ferric-based nanocomposite using the SNF as templates obtained by weak dissolution methods.

Herein, we firstly used a modified gentle enzymatical degradation method consisting of urea and guanidine hydrochloride to extract the silk fibroin (Tan et al., 2018). The nanocomposite was then designed by in situ synthesis of ferric oxides anchored to silk fibroin. The structure and morphology of the nanocomposite was characterized, and the performance for elimination of antimonite was evaluated. Finally, deep insights were focused on the antimonite binding mechanism.

2. Experimental section

2.1. Materials

All chemicals used in this study were of analytical grade. Sodium carbonate (Na_2CO_3), urea (NH_2CONH_2), guanidine hydrochloride ($NH_2C(NH)NH_2{\cdot}HCl$), Ferrous chloride tetrahydrate ($FeCl_3{\cdot}6H_2O$), sodium hydroxide (NaOH), and hydrochloric acid (HCl) were purchased from Sinopharm Chemical Reagent Co., Ltd.. Stock 1000 mg/L antimonite solution was prepared by dissolving potassium antimonyl tartrate trihydrate ($C_8H_4K_2O_{12}Sb_2{\cdot}3H_2O$, Sigma-Aldrich) in deionized water. The working antimonite solutions were freshly prepared each time by diluting the stock solutions to required concentrations.

2.2. Synthesis of SNF-ferric oxide nanohybrid

First, Bombyx mori cocoons were degummed twice in a boiling solution of 0.5 wt% Na_2CO_3, and the obtained silk fibroin was washed by distilled water for several times and dried at 50 °C for 24 h. Then, the silk fibroin was hydrolyzed and degraded by a mixture of urea and guanidine hydrochloride according to the mothed modified from previous study (Tan et al., 2018), then followed washing and filtration by distilled water. The exfoliated tofukasu-like materials were then dispersed in water with a weight ratio of 1:250 under vigorous stirring. The silk nanofibril solution was obtained after the above suspension was sonicated and centrifuged. Finally, a certain amount of 0.1 M $FeCl_3$ was added to silk nanofibril solution and stirred for half an hour, then 1 M NaOH was introduced to the suspensions drop by drop. The mixture was incubated at room temperature for two days, and then filtered, washed and dried for further use and characterization.

2.3. Batch experiments

The batch experiments were carried out to evaluate the removal performance of antimonite, including the effect of SF ligand, the effect of pH, selectivity and maximum removal capacity. Firstly, a series of nanohybrids were prepared to study the effect of SF ligand on the removal performance by adding different quantity of SNF to react with iron ions. The effect of pH was investigated in a broad pH ranging at 3, 5, 7, 9 and 11, and the pH values were adjusted by adding either HCl or NaOH solutions. The selectivity for antimonite was studied at the presence of different anions including sulfate (SO_4^{2-}), nitrate (NO_3-), carbonate (CO_3^{2-}), silicate (SiO_3^{2-}) and phosphate (PO_4^{3-}), in which the concentrations of interfering ions are three time higher than antimonite. And the adsorption isotherm studies were conducted at initial concentrations ranging from 5 to 60 mg/L, with a constant adsorbent dosage of 0.4 g/L. To obtain information on adsorption kinetics, a dosage of 0.4 g/L of adsorbent was added to a 50 mL solution containing 40 mg/L Sb(III) solutions. The suspensions were shaken for 5 min to 24 h. All the mixtures were horizontally shaken in a shaking water bath at room temperature. After equilibrium, the solids were separated from the aqueous solutions. The concentrations of supernatants were determined by inductively coupled plasma optical emission spectrometer (ICP-OES, Avio 200).

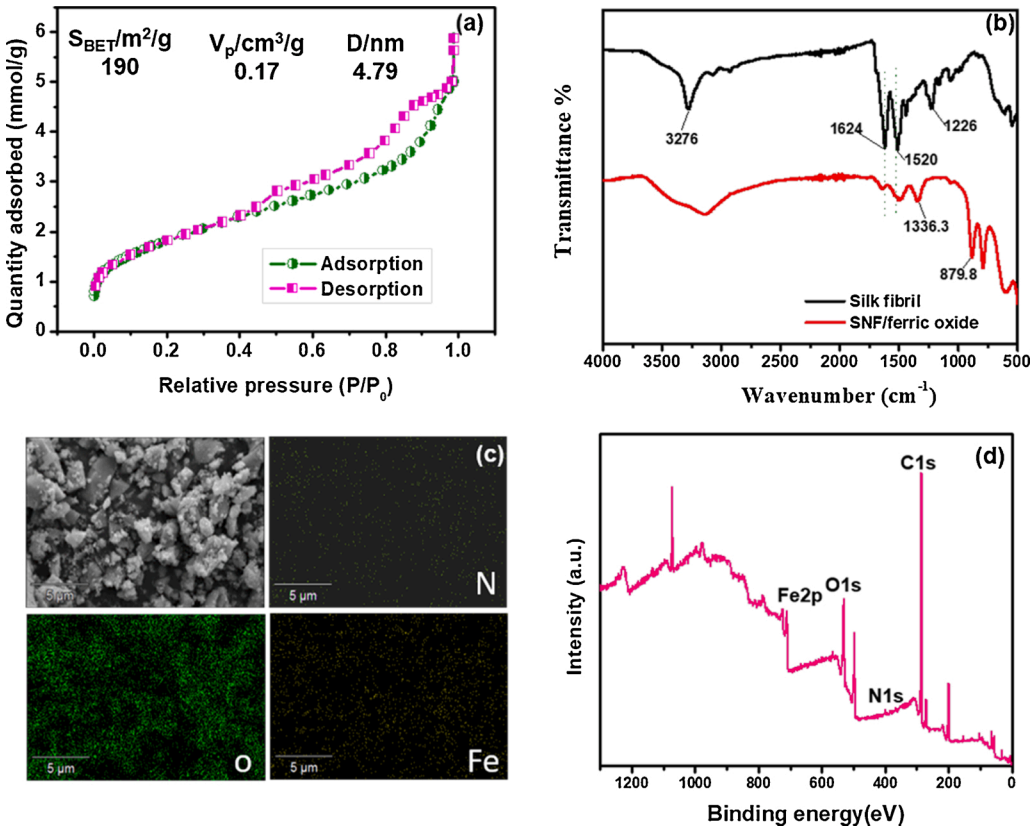

Fig. 2. (a) N_2 adsorption-desorption measurement of SNF-ferric oxide composite. (b) FTIR spectra of silk fibroin and silk fibroin-ferric oxide nanohybrid. (c) SEM image of silk fibroin-ferric oxide nanohybrid and the corresponding EDS mapping for C, O and Fe elements. (d) XPS spectra of SNF-ferric oxide nanohybrid.

2.4. Characterization

The morphologies of nano silk fibroin and silk fibroin-ferric oxide nanohybrid were studied using a transmission electron microscopy (TEM, JEM-1200EX electron microscope, JEOL, Japan), respectively. The crystal structure of the as-prepared silk fibril/ferric oxide nanocomposites were confirmed by X-ray diffraction measurements. And the element compositions of the silk fibril/ferric oxide nanocomposites were analyzed using scanning electron microscope (SEM) together with elemental mapping. The specific surface areas of the samples were examined by the Brunauer-Emmett-Teller (BET) N_2 adsorption/desorption method, and the pore size distribution was determined by the Brunauer-Joyner-Hallenda (BJH) method using desorption data. The structures and interactions of the samples before and after antimonite loading were monitored using a Fourier transform infrared spectrometer (FTIR) and an X-ray photoelectron spectroscope (XPS).

3. Results and discussion

3.1. Fabrication of SNF-ferric oxide nanohybrids

The main steps involved in the synthesis of silk fibroin-ferric oxide nanohybrids are summarized in Fig. 1a. The silk sericin was first wiped off by heating silkworms in Na_2CO_3 solutions for half an hour. A gel state material was then obtained by degrading the silk fibroin using the mixture of urea and guanidine hydrochloride (Figure S1). After washing by deionized water and filtered, the obtained tofukasu-like materials were then re-dispersed in water. The silk nanofibril (SNF) was finally obtained after the above re-dispersed solution was stirring vigorously and centrifuged (Fig. 1d). A typical sol property of Tyndall effect of the dispersion was clearly observed (Fig. 1b and 1c), suggesting the SNF was formed and homogeneously dispersed in the solution. The resulting SNF had a concentration of about 0.25 mg/mL with a relatively uniform diameter around 100 nm. The ferric nanocomposite was finally obtained by a simple pH adjustment. The SNF is rich in amino and carboxyl groups, which can coordinate with iron ions. The TEM characterization revealed that the ferric nanocomposite seemed like to have a fiber-shaped structure (Fig. 1e and Figure S2), but showing a little adhesion between the nanocomposite.

3.2. Characterization

Due to the contribution of large length-diameter ratio of the fiber-shaped nanohybrids, the specific surface area of the nanocomposite should be intriguing. The nitrogen adsorption-desorption isotherm showed that the BET surface area of the nanocomposite was 190 $m^2\ g^{-1}$, while the neat iron oxides exhibited a much lower surface area of 97.6 $m^2\ g^{-1}$. The total pore volume of the nanohybrid was 0.17 cm^3/g and the mean pore size was about 4.79 nm, exhibiting as a typical mesoporous structure (Fig. 2a). The XRD patterns exhibited four diffraction peaks at 20.6, 34.8, 61.6 and 72.8° as shown in Figure S3. The diffractive peak at around 20.6° was attributed to the sequences and conformation of amino acids onto silk fibroin, and the peaks at 34.8 and 61.6° was associated with iron oxides (Su et al., 2011; Abedini et al., 2014). It suggests the binding and coexistence of silk nanofibril and iron oxides. Additionally, the broadened reflection peaks indicate that the SNF-ferric oxide nanocomposite crystallites have small dimensions.

The mechanism about the metal-ligand binding interactions between iron ions and silk fibroin was employed by FTIR spectrum (Fig. 2b). A sharp peak at 3276 cm^{-1} was ascribed to the stack stretching vibration of N—H and OH—. The characteristic peaks responsible for the secondary structures of SF at around1624 and 1520 cm^{-1} were assigned to

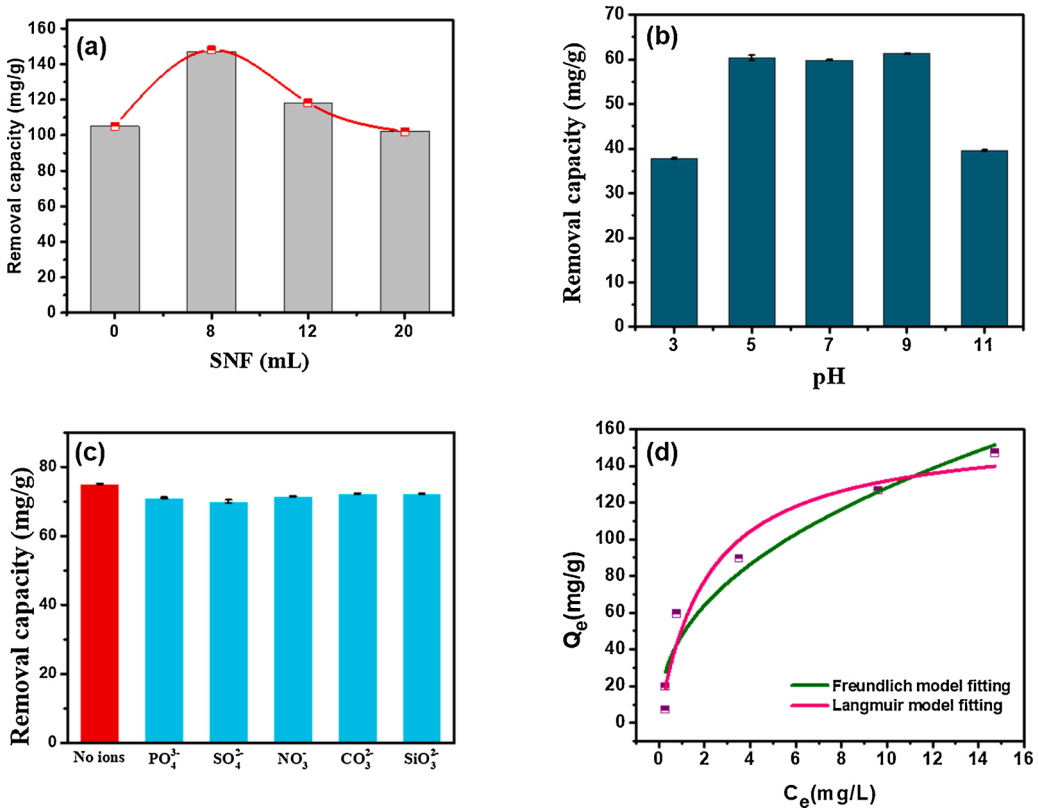

Fig. 3. Antimonite removal performance evaluation. (a) Optimum additional of SNF. (b) Effect of pH values. (c). Effect of interfering ions. (d) Fitting of the equilibrium adsorption isotherms to Langmuir and Freundlich adsorption isotherm.

β-sheets, amide I band and amide II band (Xiao and Lv, 2019; Wang et al., 2019) In the spectra of SNF/ferric oxide nanohybrid, the N—H stretching shifted to left, and the intensity of the amide II band peaks at 1624 and 1520 cm^{-1} decreased, suggesting a lower β-sheet content after chelating with iron ions. Additionally, the new peaks found at around 1336.3, 879.8 and 786.5 cm^{-1} were corresponding to Fe-O stretching (Abdullah et al., 2016; Gupta et al., 2009). The results indicated that the SF was successfully coated with ferric oxide. The compositional distribution of the elements in the nanocomposite were further assessed by means of SEM and energy dispersion spectrum (EDS) analysis, where N, O and Fe were uniformly existed in the samples (Fig. 1c). The XPS analysis was further employed to confirm the presence of C, N, O and Fe onto the nanocomposites (Fig. 1d). All the above results indicated the successful metal-ligand interactions between iron oxides and the obtained SNF.

3.3. Antimonite elimination performance assessment

3.3.1. Effect of ligand SNF

The content of SNF could influence the performance of the nanohybrids. A series of experiments were carried out by varying the SNF solution volumes to explore the positive influences of the ligand SNF on capturing of antimonite. And the ferric oxides without the addition of silk fibroin were obtained as a control. As shown in Fig. 3a, the optimal removal capacity for antimonite by the nanohybrid appeared with addition of 8 mL SNF, which was higher than the pristine ferric oxides. It demonstrated more active surface sites were available for antimonite via surface complexation after ferric oxides assembly with SNF, and the abundant amino groups could enhance the removal capacity synergistically. While the removal capacity of the nanohybrid appeared a decline with more addition of SNF. It could be ascribed that the excess of SNF could hinder the active sites of ferric oxides after the saturated metal-ligand binding interactions between iron ions and silk nanofibril.

3.3.2. Effect of pH values

The pH-dependent antimonite removal properties by the SNF/ferric nanohybrids were tested at pH values ranging from 3.0 to 11.0 (Fig. 3b). The results showed that the SNF/ferric nanohybrids exhibited superior antimonite removal capacities at a wide pH range from 5.0 to 9.0 after contacting for 24 h, while having a minor decline at a very acidic or basic condition (Fig. 3b). This is distinguishing to the reported previous works that the removal of antimonite species was generally independent on pH values due to the low electrostatic interactions involving the neutral form of H_3SbO_3 (Qi et al., 2019; Zeng et al., 2020; Xiong et al., 2020). The decline of the removal capacity was due to the possible hydrolysis reactions for part of the amino and carboxyl groups onto silk fibroins at a relatively acid or alkaline conditions.

3.3.3. Selectivity assessment

It is crucial to estimate the removal selectivity for antimonite purification in real practical applications, due to the ubiquitous anionic species in the aqueous environment. The effect of common anions including SO_4^{2-}, NO_3-, CO_3^{2-}, SiO_3^{2-} and PO_4^{3-} on the elimination of antimonite were determined. As shown in Fig. 3c, the ferric nanocomposite displays high selectivity toward antimonite at the presence of SO_4^{2-}, NO_3-, CO_3^{2-}, SiO_3^{2-} and PO_4^{3-}, in which the removal capacity was as high as that without these interfering ions even when the concentrations of interfering ions are triple higher than antimonite. Although these coexisting anions could also be adsorbed on the nanocomposite by hydrogen bonding, the removal capacity for antimonite was still not significantly affected by the anions. This is mainly due to that the synergistic effect of silk fibroin and iron oxides contributed to the superior removal ability of antimonite. The removal ability for antimonite by silk fibroin was also studied as shown in Figure S4, and it demonstrated a removal capacity of 16.3 mg/g at initial concentration of 40 mg/L and at an adsorbent dosage of 0.4 g/L. The removal capacity of antimonite by silk fibroin was much lower than the nanocomposite (Figure S4 and

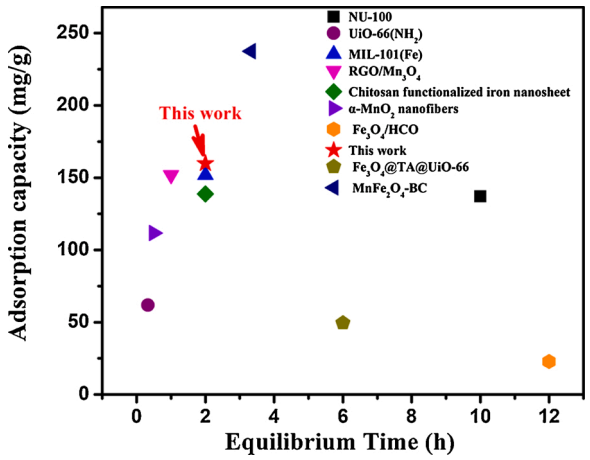

Fig. 4. Comparison of removal capacities of antimonite based on recent reported materials.

Fig. 3d), these experiments suggest the contribution of iron oxides on the removal ability was dominant. And the remarkable selectivity can be ascribed to the formed strong inner-sphere complexation between antimonite species and the SNF-ferric nanocomposite. These results confirmed the exceptional selectivity of the SNF/ferric oxide nanocomposite for antimonite removal.

3.3.4. *Comparison of removal performance*

Benefiting from the successful binding of silk nanofibril and iron oxides, the fiber-shaped nanocomposite with fascinating length-to-diameter ratio exhibited a larger surface area than the neat iron oxides. And more functional groups such as amino and carboxyl groups ascribed to silk fibroin were available on the nanocomposite, thus the silk fibroin-ferric oxide nanocomposite could present an intriguing removal capacity for antimonite. The kinetic studies were firstly performed at a predetermined time interval. The removal capacity toward antimonite remarkably increased at the initial contact stage, and reached equilibrium then followed a platform after 2 h (Figure S5). The maximum removal capacity for antimonite was then further evaluated by adsorption isotherms, which were carried out at neutral pH value with the antimonite concentration ranging from 2 to 60 mg/L. As

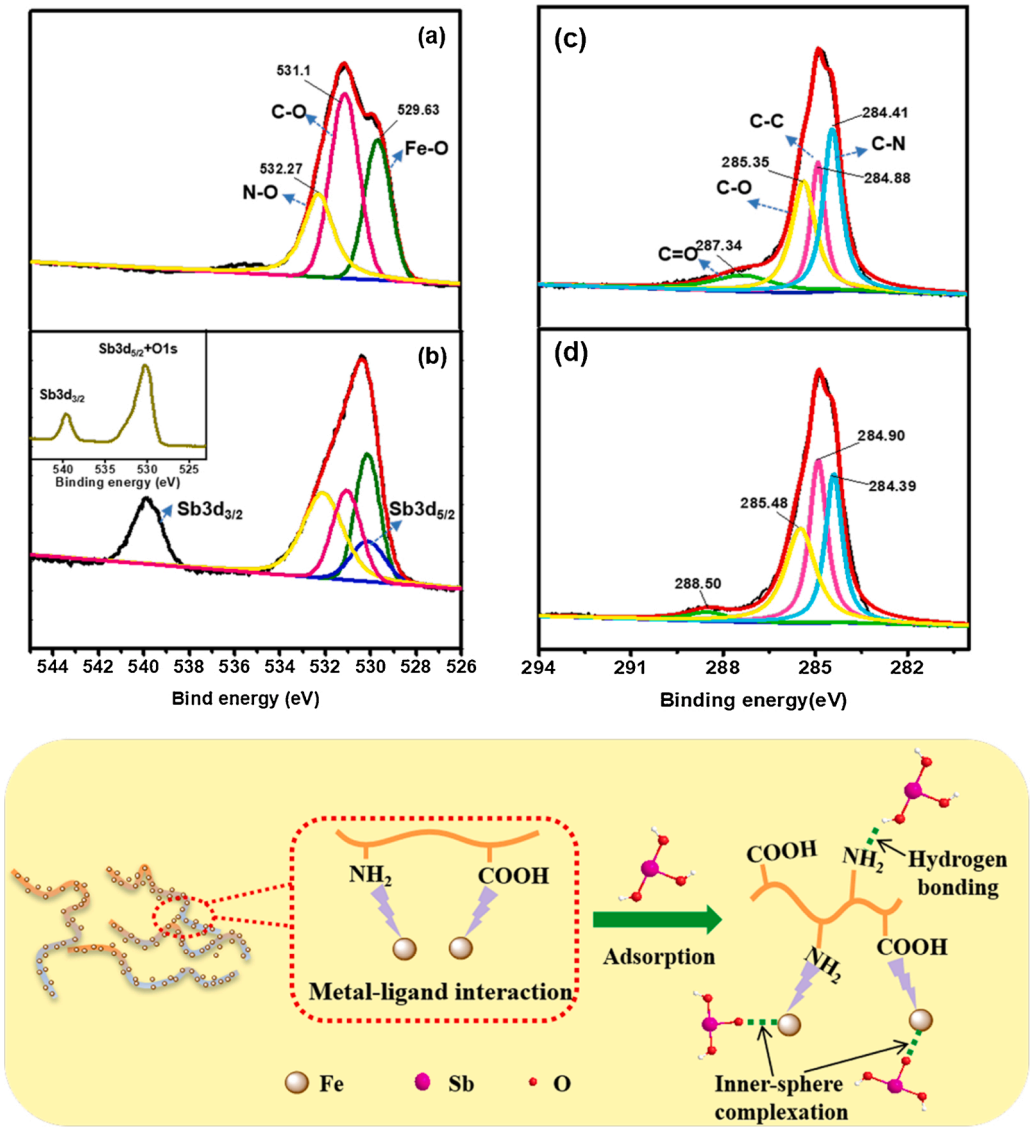

Fig. 5. O1 s spectra of the SNF-ferric oxide nanocomposite before (a) and after loading of antimonite (b). C1 s spectra of the SNF-ferric oxide nanocomposite before (c) and after loading of antimonite (d). (e) Schematic illustration for the antimonite binding mechanism onto the nanohybrid.

illustrated in Fig. 2d, the removal of antimonite was preferred by the Langmuir model with the correlation coefficient $R^2 > 0.96$ (Table S1), suggesting that the adsorption procedure is monolayer. The theoretical maximum adsorption capacity calculated by Langmuir model was 159.9 mg/g. The high removal capacity was ascribed to the increment of the specific surface area provided during the self-assembly process of ferric oxide and silk fibroin, as well as the substantial functional groups available on silk fibroin. To our knowledge, this SNF-ferric oxide nanocomposite showed relatively better removal capacity than most of the recent reported nanocomposite materials, including porous MOFs, nanofiber-based materials and magnetic nanocomposites (Fig. 4) (Qi et al., 2019; Li et al., 2017; Zeng et al., 2020; He et al., 2017; Zhang et al., 2019b; Zou et al., 2016; Wang et al., 2018b; Luo et al., 2017b; Zhang et al., 2019c). In particular, except for the high removal capacity and selectivity, both silk fibroin and iron oxide are environmental-friendly.

3.4. Binding mechanisms

To gain further insights into the removal mechanism, X-ray photoelectron spectroscopy (XPS) were performed to analyze the chemical binding energy of SNF-ferric oxide nanohybrid before and after antimonite loading. The C1 s, N1 s, O1 s and Fe 2p were existed in the survey scan spectrum of the nanocomposite as shown in Figure S6, in which N1 s was obviously from the SNF components. A much stronger and distinct peak located at around 540 eV was observed for antimonite-loaded samples, resulting from the contribution of O1 s and the adsorbed antimonite (at these two peaks are very close). It suggests successful antimonite scavenge by the nanocomposite. The Sb 3d speaks of the nanocomposite after adsorption display two representative peaks centering at about 540 eV (Sb $3d_{3/2}$) and 530.2 eV (Sb $3d_{5/2}$) (the inset in Fig. 5b), which demonstrates the presence of antimonate (higher binding energy) and antimonite (lower binding energy), respectively (Hudcová et al., 2019). The observed two typical peaks corresponding to $Sb3d_{3/2}$ and $Sb3d_{5/2}$ suggest partial oxidation of antimonite to antimonate.

The deconvolution of O1 s and C1 s spectra was further explored, respectively. The O1 s peak consisted of the contributions of N–O, CO and FeO——. A shift for the peak at around 530.1 eV with loaded antimonite may be ascribed to the surface complexation binding of Fe—O and Sb (Fig. 5a and b). Overall consideration of the powerful selectivity of the nanohybrids, the antimonite could be captured via the formation of inner-sphere complexes. The reduction of peak areas centering around 532.2 and 531.1 eV could be attributed to the weak hydrogen bonds formed between the antimonite species and the amino/carboxyl groups onto silk fibril. And the right shift of the binding energy at around 285.3 and 287.3 eV for C 1s also indicates the formation of hydrogen bonds (Fig. 5c and d).

The confirmation of involved removal mechanism was further explored by FTIR analysis (Figure S7), in which the peaks at 1495.8 and 1341.8 cm^{-1} corresponding to amido and Fe—O stretching were decreased after antimonite coverage. This result also suggest that the capture of antimonite species is dominantly controlled by the synergistic effect of surface complexation and hydrogen bonding. To summarize the above analysis, Fig. 5e demonstrates the related removal mechanism of antimonite onto the SNF-ferric oxide nanohybrid. The functional groups onto silk fibroin can stack and assembly with iron ions by metal-ligand binding interactions, in which the fiber-shaped nanohybrids with high length-diameter ratio and high surface areas can offer more active sites. According to XPS and FTIR spectra analysis as well as the macroscopic experiments, the antimonite species were attached onto Fe-O bonds mainly via the formation of strong surface complexation. And the abundant carboxyl and amino groups also contributed to the elimination of antimonite by the formation of hydrogen bonds. Overall, the environmental-friendly nanohybrid might be a promising material for antimonite elimination with high selectivity and excellent removal capacity.

4. Conclusion

In summary, we developed a novel fiber-shaped nanohybrid by anchoring ferric oxides on silk nanofibril. The exfoliated SNF possessed uniform fiber diameter after enzymatic degradation. The ferric oxide in situ grew along the silk nanofibril via metal-ligand binding interaction, and the obtained nanohybrids inherited both the functions of ferric oxide and silk nanofibril. The as-prepared nanohybrids achieved an excellent antimonite removal capacity of 159.9 mg/g, which was superior than most reported kinds of materials to our knowledge. Moreover, the nanohybrid showed high selectivity in the presence of anionic species of SO_4^{2-}, NO_3-, CO_3^{2-}, SiO_3^{2-} and PO_4^{3-}. The over consideration of high adsorption capacity, environmental-friendly and high selectivity, the novel fiber-shaped silk fibroin-ferric oxide nanohybrid developed in this study would be promising materials for antimonite extraction from water.

CRediT authorship contribution statement

Pengfei Qi: Conceptualization, Methodology, Data curation, Writing - original draft, Writing - review & editing, Visualization, Funding acquisition. **Jianqiang Zeng:** Formal analysis, Investigation, Visualization. **Xiaohua Tong:** Investigation, Visualization. **Junjie Shi:** Writing - review & editing. **Yan Wang:** Writing - review & editing. **Kunyan Sui:** Supervision.

Declaration of Competing Interest

The authors reported no declarations of interest.

Acknowledgements

This research was supported by Natural science foundation of Shandong Province (ZR2019QD019), and Program for Taishan Scholar of Shandong Province.

Appendix A. Supplementary data

Supplementary material related to this article can be found, in the online version, at doi:https://doi.org/10.1016/j.jhazmat.2020.123909.

References

Abedini, A., Daud, A.R., Hamid, M.A.A., Othman, N.K., 2014. Radiolytic formation of Fe_3O_4 nanoparticles: influence of radiation dose on structure and magnetic properties. PLoS One 9, e90055.

Abdullah, N., Gohari, R.J., Ismail, A.F., Juhana, J., Lau, W.J., Matsuura, T., 2016. Polysulfone/hydrous ferric oxide ultrafiltration mixed matrix membrane: preparation, characterization and its adsorptive removal of lead(II) from aqueous solution. Chem. Eng. J. 289, 28–37.

Fei, X., Shao, Z., Chen, X., 2013a. Hematite nanostructures synthesized by a silk fibroin-assisted hydrothermal method. J. Mater. Chem. B 1, 213–220.

Fei, X., Shao, Z., Chen, X., 2013b. Synthesis of hierarchical three-dimensional copper oxide nanostructures through a biomineralization-inspired approach. Nanoscale 5, 7991–7997.

Gupta, A., Chauhan, V.S., Sankararamakrishnan, N., 2009. Preparation and evaluation of iron–chitosan composites for removal of As(III) and As(V) from arsenic contaminated real life groundwater. Water Res. 43, 3862–3870.

Gore, P.M., Naebe, M., Wang, X., Kandasubramanian, B., 2019. Progress in silk materials for integrated water treatments: fabrication, modification and applications. Chem. Eng. J. 374, 437–470.

He, X., Min, X., Luo, X., 2017. Efficient removal of antimony(III, V) from contaminated water by amino modification of zirconium metal-organic framework with mechanism study. J. Chem. Eng. Data 62, 1519–1529.

Hudcová, B., Erben, M., Vítková, M., Komárek, M., 2019. Antimonate adsorption onto Mg-Fe layered double hydroxides in aqueous solutions at different pH values: coupling surface complexation modeling with solid-state analyses. Chemosphere 229, 236–246.

Li, J., Li, X., Hayat, T., Alsaedi, A., Chen, C., 2017. Screening of zirconium-based metal-organic frameworks for efficient simultaneous removal of antimonite (Sb(III)) and antimonate (Sb(V)) from aqueous solution. ACS Sustain. Chem. Eng. 5, 11496–11503.

Li, J., Wang, X., Zhao, G., Chen, C., Chai, Z., Alsaedi, A., Hayat, T., Wang, X., 2018. Metal–organic framework-based materials: superior adsorbents for the capture of toxic and radioactive metal ions. Chem. Soc. Rev. 47, 2322–2356.

Liu, Y., Wu, P., Liu, F., Li, F., An, X., Liu, J., Wang, Z., Shen, C., Sand, W., 2019. Electroactive modified carbon nanotube filter for simultaneous detoxification and sequestration of Sb(III). Environ. Sci. Technol. 53, 1527–1535.

Luo, J., Hu, C., Meng, X., Crittenden, J., Qu, J., Peng, P., 2017a. Antimony removal from aqueous solution using novel α-MnO_2 nanofibers: equilibrium, kinetic, and density functional theory studies. ACS Sustain. Chem. Eng. 5, 2255–2264.

Luo, J., Hu, C., Meng, X., Crittenden, J., Qu, J., Peng, P., 2017b. Antimony removal from aqueous solution using novel α-MnO_2 nanofibers: equilibrium, kinetic, and density functional theory studies. ACS Sustain. Chem. Eng. 5, 2255–2264.

Mi, R., Liu, Y., Chen, X., Shao, Z., 2016. Structure and properties of various hybrids fabricated by silk nanofibrils and nanohydroxyapatite. Nanoscale 8, 20096.

Pan, B., Chen, D., Zhang, H., Wu, J., He, F., Wang, J., Chen, J., 2018. Stability of hydrous ferric oxide nanoparticles encapsulated inside porous matrices: effect of solution and matrix phase. Chem. Eng. J. 347, 870–876.

Qi, P., Luo, R., Pichler, T., Zeng, J., Wang, Y., Fan, Y., Sui, K., 2019. Development of a magnetic core-shell Fe_3O_4@TA@UiO-66 microsphere for removal of arsenic(III) and antimony(III) from aqueous solution. J. Hazard. Mater. 378, 120721.

Rockwood, D.N., Preda, R.C., Yücel, T., Wang, X., Lovett, M.L., Kaplan, D.L., 2011. Materials fabrication from Bombyx mori silk fibroin. Nat. Prot. 6, 1612–1631.

Samal, S.K., Dash, M., Shelyakova, T., Declercq, H.A., Uhlarz, M., Manuel, B.-L., Dubruel, P., Cornelissen, M., Herrmannsdörfer, T., Rivas, J., Smedt, S.D., Braeckmans, K., Kaplan, D.L., Dediu, V.A., 2015. Biomimetic magnetic silk scaffolds. ACS Appl. Mater. Interfaces 7, 6282–6292.

Sheng, W., Liu, J., Liu, S., Lu, Q., Kaplan, D.L., Zhu, H., 2014. One-step synthesis of biocompatible magnetite/silk fibroin core-shell nanoparticles. J. Mater. Chem. B 2, 7394–7402.

Shi, C., Xing, Y., Patil, A., Meng, Z., Yu, R., Lin, N., Qiu, W., Hu, F., Liu, X., 2019. Primary and secondary mesoscopic hybrid materials of Au Nanoparticles@Silk fibroin and applications. ACS Appl. Mater. Interfaces 11, 30125–30136.

Su, H., Han, J., Dong, Q., Xu, J., Chen, Y., Gu, Y., Song, W., Zhang, D., 2011. In situ bioinspired synthesis of silver chloride nanocrystals on silk fibroin fibers. Appl. Phys. A 102, 429–434.

Tan, X., Zhao, W., Mu, T., 2018. Controllable exfoliation of natural silk fibers into nanofibrils by protein denaturant deep eutectic solvent: nanofibrous strategy for multifunctional membranes. Green Chem. 20, 3625–3633.

Ungureanu, G., Santos, S., Boaventura, R., Botelho, C., 2015. Arsenic and antimony in water and wastewater: overview of removal techniques with special reference to latest advances in adsorption. J. Environ. Manage. 151, 326–342.

Wang, L., Wan, C., Lee, D.-J., Liu, X., Zhang, Y., Chen, X.F., Tay, J.-H., 2014. Biosorption of antimony(V) onto Fe(III)-treated aerobic granules. Biol. Technol. 158, 351–354.

Wang, Y., Guo, J., Zhou, L., Ye, C., Omenetto, F.G., Kaplan, D.L., Ling, S., 2018a. Design, fabrication, and function of silk-based nanomaterials. Adv. Funct. Mater. 28, 1805305.

Wang, Y.-Y., Ji, H.-Y., Lu, H.-H., Liu, Y.-X., Yang, R.-Q., He, L.-L., Yang, S.-M., 2018b. Simultaneous removal of Sb(III) and Cd(III) in water by adsorption onto a $MnFe_2O_4$–biochar nanocomposite. RSC Adv. 8, 3264–3273.

Wang, Z., Yang, H., Zhu, Z., 2019. Study on the blends of silk fibroin and sodium alginate: hydrogen bond formation, structure and properties. Polymer 163, 144–153.

Wei, Y., Wei, S., Liu, C., Chen, T., Tang, Y., Ma, J., Yin, K., Luo, S., 2019. Efficient removal of arsenic from groundwater using iron oxide nanoneedle array-decorated biochar fibers with high Fe utilization and fast adsorption kinetics. Water Res. 167, 115107.

Xiao, M., Lv, S., 2019. Self-assembled regenerated silk fibroin microsphere-embedded Fe_3O_4 magnetic nanoparticles for immobilization of zymolyase. ACS Omega 4, 21612–21619.

Xiong, N., Wan, P., Zhu, G., Xie, F., Xu, S., Zhu, C., Hursthouse, A.S., 2020. Sb(III) removal from aqueous solution by a novel nano-modified chitosan (NMCS). Sep. Purif. Technol. 236, 116266.

Xue, J., Gao, H.L., Wang, X.Y., Qian, K.Y., Yang, Y., He, T., He, C., Lu, Y., Yu, S.H., 2019. Bioinspired unidirectional silk fibroin-silver compound nanowire composite scaffold via interface-mediated in situ synthesis. Angew. Chem. Int. Ed. 131, 14290–14294=.

Zeng, J., Qi, P., Shi, J., Pichler, T., Wang, F., Wang, Y., Sui, K., 2020. Chitosan functionalized iron nanosheet for enhanced removal of As(III) and Sb(III): synergistic effect and mechanism. Chem. Eng. J. 382, 122999.

Zhang, Q., Bolisetty, S., Cao, Y., Handschin, S., Adamcik, J., Peng, Q., Mezzenga, R., 2019a. Selective and efficient removal of fluoride from water: in situ engineered amyloid Fibril/ZrO_2 hybrid membranes. Angew. Chem. Int. Ed. 58, 6012–6016.

Zhang, W., Li, N., Xiao, T., Tang, W., Xiu, G., 2019b. Removal of antimonite and antimonate from water using Fe-based metal-organic frameworks: the relationship between framework structure and adsorption performance. J. Environ. Sci. 86, 213–224.

Zhang, J., Deng, R.-j., Ren, B.-z., Hou, B., Hursthouse, A., 2019c. Preparation of a novel Fe_3O_4/HCO composite adsorbent and the mechanism for the removal of antimony (III) from aqueous solution. Sci. Rep. 9, 1–11.

Zhao, T., Tang, Z., Zhao, X., Zhang, H., Wang, J., Wu, F., Giesy, J.P., Shi, J., 2019. Efficient removal of both antimonite (Sb(iii)) and antimonate (Sb(v)) from environmental water using titanate nanotubes and nanoparticles. Environ. Sci.-Nano 6, 834–850.

Zou, J.-P., Liu, H.-L., Luo, J., Xing, Q.-J., Du, H.-M., Jiang, X.-H., Luo, X.-B., Luo, S.-L., Suib, S.L., 2016. Three-dimensional reduced graphene oxide coupled with Mn_3O_4 for highly efficient removal of Sb(III) and Sb(V) from water. ACS Appl. Mater. Interfaces 8, 18140–18149.